Origami-Based Bistable Metastructures for Low-Frequency Vibration Control

Mingkai Zhang
School of Aerospace Engineering,
Beijing Institute of Technology,
Beijing 100081, China
e-mail: mkzhang@bit.edu.cn

Jinkyu Yang
Department of Aeronautics and Astronautics,
University of Washington,
Seattle, WA 98195
e-mail: jkyang@aa.washington.edu

Rui Zhu[1]
School of Aerospace Engineering,
Beijing Institute of Technology,
Beijing 100081, China
e-mail: ruizhu@bit.edu.cn

In this research, we aim to combine origami units with vibration-filtering metastructures. By employing the bistable origami structure as resonant unit cells, we propose metastructures with low-frequency vibration isolation ability. The geometrical nonlinearity of the origami building block is harnessed for the adjustable stiffness of the metastructure's resonant unit. The quantitative relationship between the overall stiffness and geometric parameter of the origami unit is revealed through the potential energy analysis. Both static and dynamic experiments are conducted on the bistable origami cell and the constructed beam-like metastructure to verify the adjustable stiffness and the tunable vibration isolation zone, respectively. Finally, a two-dimensional (2D) plate-like metastructure is designed and numerically studied for the control of different vibration modes. The proposed origami-based metastructures can be potentially useful in various engineering applications where structures with vibration isolation abilities are appreciated. [DOI: 10.1115/1.4049953]

Keywords: origami, metastructure, vibration control, bistable, wave propagation

1 Introduction

Metamaterials are materials with unique properties that are not found in natural materials, which were first introduced in the electromagnetic field [1]. Then, they have expanded to the field of acoustic and elastic waves [2,3]. By designing the subwavelength-scale microstructure, elastic metamaterial can possess peculiar effective properties, such as negative mass density/bulk modulus [4–6] and odd elasticity [7–9]. As the metamaterial-based finite structures, metastructures possess excellent vibration isolation ability, especially in the low-frequency range [10,11], which can be very beneficial in aerospace and automotive industries where engineering structures with simultaneous lightweight and vibration-proof abilities are much appreciated [12,13].

Comparing with the Bragg scattering-based phononic crystals, elastic metamaterials/metastructures can have extremely low-frequency bandgap that stops long-wavelength wave propagation. Simple mass–spring models can clearly explain the local resonance mechanism which introduces a negative effective mass density inside the bandgap region [14]. Based on this, various metastructure designs were proposed specifically for low-frequency vibration isolation in some representative engineering structures such as bar, beam, and plate. Yu et al. investigated flexural vibration isolation in a Timoshenko beam with ring-like local resonators [15]. Zhu et al. investigated a cantilever-mass locally resonant microstructure which is manufactured by laser cutting a single-phase plate, and a low-frequency bandgap in both in-plate and out-of-plate guided waves was achieved [16]. Miranda et al. studied a plate-like metastructure with three-dimensional (3D)-printed local resonators [17]. However, the unadjustable resonators fix the metastructures' bandgaps which are often too narrow to be useful in many practical applications.

To solve the narrow bandgap problem, multi-resonator designs were proposed in passive metastructures. Pai designed a bar-like metastructure with different spring–mass absorbers separated into multiple sections to achieve broadband wave absorption [18]. Chen et al. theoretically demonstrated that frequency range for wave mitigation and/or absorption can be enlarged by introducing interior dissipative multi-resonators in beam-like metastructures [19]. The multi-resonator designs sacrifice the overall weight of the metastructures to achieve the desired broadband purpose. On the other hand, tunable resonator designs in active metastructures can avoid added weight or remanufacturing and therefore, are more suitable for real engineering applications. One way to achieve tunability is to introduce shunted piezoelectric materials and control circuits into the metastructures [20–23]. Zhu et al. experimentally investigated the tunable dynamic behavior of a metastructure, which is actively controlled by negative capacitance piezoelectric shunting [22]. Li et al. designed a self-adaptive beam-like metastructure that is digitally controlled for broadband flexural wave attenuation [23]. However, active metastructures with piezoelectric shunting require complicated circuit fabrications and, therefore, lead to high costs in realization. In order to avoid any complexity associated with electromechanical or magneto-mechanical coupling while still achieving the desired metastrutures' tunability, new designs of reconfigurable microstructure in a full mechanical context need to be considered.

Origami is a paper folding technique and becomes an emerging research frontier due to its ability to transform two-dimensional (2D) flat sheets into 3D complex structures with reconfigurable abilities [24–27]. The overall mechanical properties of a 3D origami structure can be programed by its pattern of crease, which introduces various interesting mechanical properties, such as tunable stiffness, multistability, and coupled deformations [28–31]. Once obtaining the knowledge about the properties of the side plates, the creases, and the folding procedure, the mechanical response of the 3D origami structure can be completely determined. Therefore, origami with highly designable and tunable abilities offers new possibilities for functional metastructures. Previous origami-based metastructure designs have demonstrated that they can provide desired static as well as dynamic characteristics [32,33]. However, there are few studies on the dynamic properties, especially the vibration controllability, of the origami metastructures.

In this paper, we first designed a prismatic origami unit and analyzed its mechanical response based on the minimum energy principle. Special attentions were paid on the relationship between the adjustable stiffness and geometric parameters of the origami unit. Then, based on the Timoshenko beam theory and transfer matrix

[1]Corresponding author.

Manuscript received October 2, 2020; final manuscript received January 22, 2021; published online February 23, 2021. Assoc. Editor: Pedro Reis.

method, theoretical modeling of a beam-like metastructure with the origami-based resonant unit was proposed. Tunable bandgap was obtained based on the bistable origami unit with adjustable stiffness. Subsequently, both numerical and experimental investigations were performed on the origami-based metastructure for vibration suppression purposes. Finally, we extended the one-dimensional (1D) beam-like metastructure to the 2D plate-like metastructure and numerically proved its ability in the control of vibration modes.

2 Microstructure Design and Experimental Validation of the Bistable Origami Unit

In this section, the kinematics of the origami unit is first investigated. Then, a theoretical model is developed to obtain the mechanical behavior of the origami unit. Finally, tunable mechanical behavior as well as the bistability of the origami unit are validated experimentally.

2.1 Origami Unit and Metastructure. Figure 1(*a*) shows the geometry of the unfolded origami structure which can be defined by three parameters. The first one is the circumradius of the regular polygon R. Then, N is used to define the number of sides of the polygon. The angle between OB (the line between the vertex and the center of the circle) and BA (the edge of the polygon) is given by $\alpha = \pi/2 - \pi/N$, while the angle between CA (the diagonal of parallelograms) and AB is β. Therefore, the last parameter is defined as $\lambda = \beta/\alpha$. By folding and pasting, the flat 2D pattern can be transformed into the 3D origami unit, a polygonal twisted prism whose top and bottom surfaces are regular polygons surrounded by parallelograms. Each parallelogram can be divided into a pair of triangles with a crease along its diagonal and a slit between each pair of adjacent parallelograms. These slits play important roles in the kinematics of the 3D origami since they provide the structure with freely bendable edges. By changing the parameters N and λ, one can obtain various 3D origami units with monostable or bistable abilities, as shown in Fig. 1(*b*). By arranging the local resonators, which are manufactured with the origami units and metal discs, onto a metal beam, an origami-based beam-like metastructure is formed and its vibration isolation ability is about to be investigated. With the proposed origami unit as the key part of the metastructure's cell, bistability-induced tunable bandgaps as well as

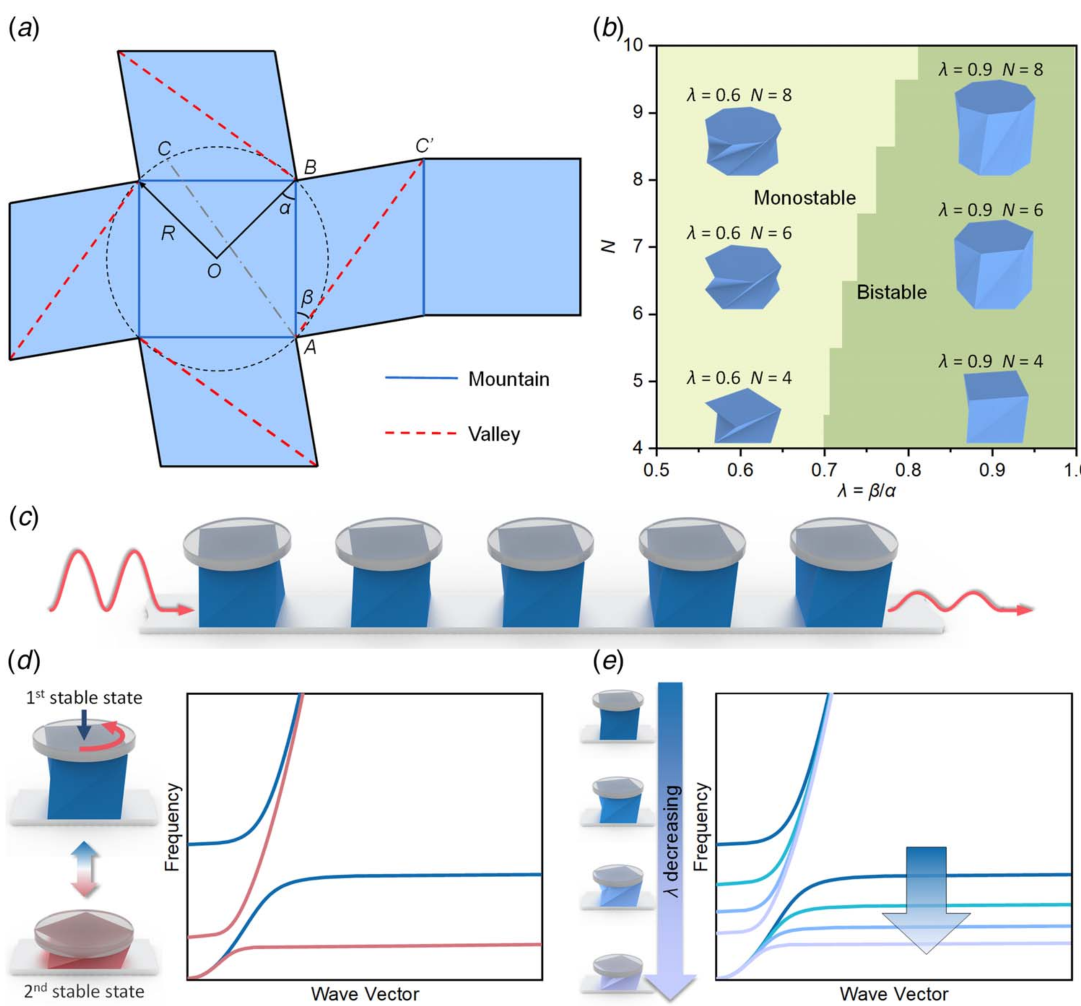

Fig. 1 Designed tunable origami-based metastructure. (*a*) Unfolded origami unit with crease patterns consisting of mountain crease lines (shown as blue solid lines) and valley crease lines (shown as red dashed lines). (*b*) Design space of the origami unit. Several origami units with varying *N*, λ are listed in the illustration. The origami units with the geometric parameters represented by the left region are monostable structures. The bistable structures are on the right. (*c*) Origami units are introduced into the metastructure which has excellent vibration isolation. (*d*) The bandgap can be easily tuned by switching stable state. (*e*) By reducing λ, bandgap moves to a lower frequency range.

parameter λ-controlled band structures are expected, as shown in Figs. 1(*d*) and 1(*e*), respectively.

2.2 Theoretical Modeling of the Origami Unit. For the kinematics of the 3D origami, the twist movements of the two surfaces are coupled with their axial motions. Therefore, under the axial deformation of the 3D origami, the triangular side plates undergo bending and the overall structure demonstrates a complex twist coupling deformation mode. In order to facilitate the following theoretical modeling and analysis, reasonable geometric constraints are introduced into the deformation processes of the origami structures. (1) The top and bottom two polygonal plates remain flat and are only allowed to rotate about the vertical axis during the deformation process. (2) The diagonal creases of the parallelograms remain straight, and the length remains constant. (3) The free edge of the triangular plate can be freely bent to form an arbitrary 3D curve, but the total length remains unchanged because the surface of the triangular plate is assumed to be a developable surface. In order to study the static properties of the proposed origami, a theoretical model is developed to calculate the variation of energy in an origami structure during deformation. Finally, we establish the relationship between the potential energy and the geometrical parameters. Here, all surfaces of the structure are assumed to have a uniform thickness, and the total energy in the structure is divided into two parts, one part of the energy is stored in the freely curved triangular panels which are modeled as shells, while the other part of the energy is stored in the creases which are modeled as torsion springs. The total system energy (E_{T}) actually is the sum of the bending energy (E_{B}) of the panels and the energy stored in the creases (E_{C}). The mechanical behavior of the origami structure is determined by the deformation of the panels and the creases. Due to symmetry, we just need to study the potential energy of the single parallelogram side instead of whole structure which includes two panels and three creases, as shown in Fig. 2(*a*).

To calculate the bending energy of the panels, we first need to obtain the shape of the panels at each instantaneous height during the compression process. At the initial state, all panels are flat which can be described as plane with a constant Gaussian curvature equal to zero in mathematics. We assume that the panels subjected to pure bending throughout the compression process which means that the Gaussian curvature of the panels remains constant during compression. So that the panels can be described as developable surface at each instantaneous height. Here, generalized cones are used to describe the triangular plates, and the governing pair of space curves $\mathbf{R}_{BB^i}(u)$ are the free edge of the triangular panel which can be described by Bezier curves, as shown in Fig. 2(*c*). The free edge of each triangular panel in the local coordinate system can be represented as

$$\mathbf{R}_{BB^i}(u) = [B_x(u), B_y(u), 0] \tag{1}$$

where

$$\begin{cases} B_x(u) = 2u(1-u)p_x + u^2 l_{BB^i} \\ B_y(u) = 2u(1-u)p_y \end{cases} \tag{2}$$

l_{BB^i} is the length of the line segment BB^i. p_x, p_y are the pending parameters that are used to describe the Bezier curve. Since the length of the free edge remains the same, the Bezier curve should satisfy the following equation:

$$\int_{\mathbf{R}_{BB^i}} ds = L_C \tag{3}$$

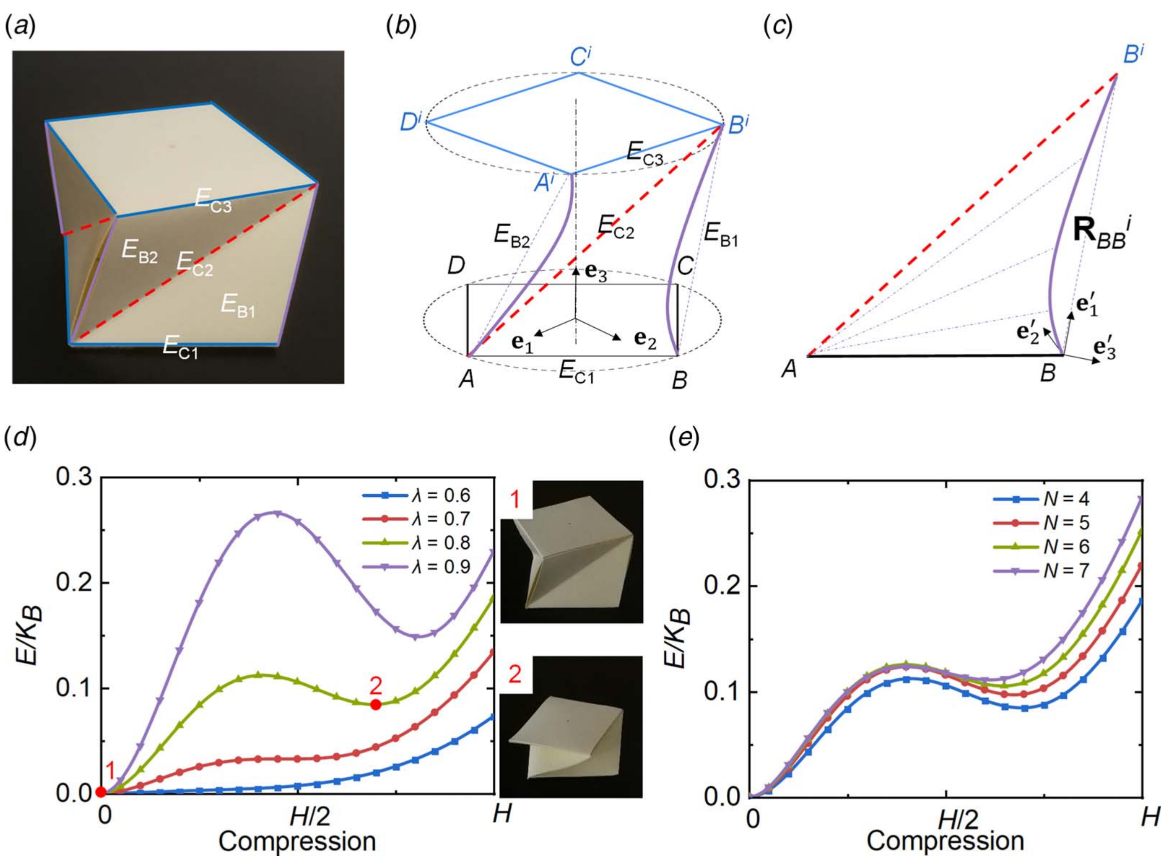

Fig. 2 (*a*) The energy distributions in different structural components of a unit cell. (*b*) Creases are modeled as linear torsion springs. (c) Triangular panels are modeled as developable surfaces. (*d*) The energy–compression curve of origami structures for different λ, and (e) The energy–compression curve of origami structures for different *N*. (Color version online.)

The local coordinate system $(\mathbf{e}_1', \mathbf{e}_2', \mathbf{e}_3')$ is defined as follows:

$$\mathbf{e}_1' = \frac{\boldsymbol{BB^i}}{|\boldsymbol{BB^i}|}, \quad \mathbf{e}_2' = \frac{\boldsymbol{AB} \times \boldsymbol{AB^i}}{|\boldsymbol{AB} \times \boldsymbol{AB^i}|}, \quad \mathbf{e}_3' = \mathbf{e}_1' \times \mathbf{e}_2' \tag{4}$$

The surface ABB^i can be described by the following parametric equation:

$$\mathbf{R}_{ABB^i}(u, v) = \mathbf{A} + v(\mathbf{R}_{BB^i}(u) - \mathbf{A}), \quad u \in [0, 1], \quad v \in [0, 1] \tag{5}$$

The bending energy of a developable surface can be expressed as a function of the surface integral of the squared mean curvature. Thus, for the two triangular panels shown in Fig. 2(*b*)

$$E_B = K_B \iint [H^2_{ABB^i}(u, v) + H^2_{B^iA^iA}(u, v)] dS \tag{6}$$

where K_B is the is the bending rigidity of the panels which is a function of Young's modulus, Poisson's ratio, and material thickness; $H_{ABB^i}(u, v)$ and $H_{B^iA^iA}(u, v)$ are mean curvatures of the two surfaces ABB^i and B^iA^iA, respectively. During compression, the instantaneous fold angle of the creases is calculated and the energy stored in the creases is proportional to the square of the deviation in the angle from the rest position.

Next, we discuss the part of the energy stored in the crease in Fig. 2(*b*). For the crease energy calculation, we consider the creases to be linear elastic torsional springs. The stiffness of the creases (K_C) was obtained by experimental measurement, and the detailed process is shown in Appendix A. The energy stored in the creases is proportional to the square of the difference between initial and instantaneous angles. Taking the crease AB as an example, the energy stored in it can be calculated as

$$(E_C^{AB})_{h_i} = \frac{K_C}{2} \int_A^B [(\varphi_{AB})_{h_i} - (\varphi_{AB})_{h_0}]^2 dl \tag{7}$$

where $(\varphi_{AB})_{h_i}$ is the instantaneous fold angle of the crease AB and $(\varphi_{AB})_{h_0}$ is the initial angle. Each side of the origami structure has three creases, so the crease energy stored in the single side shown in Fig. 2(*b*) can be expressed as

$$E_C = (E_C^{AB})_{h_i} + (E_C^{AB^i})_{h_i} + (E_C^{A^iB^i})_{h_i} \tag{8}$$

Thus, the total energy of an origami structure with N sides can be written as

$$E_T = N(E_B + E_C) \tag{9}$$

According to the minimum energy principle, we can get the shape and energy of the origami structures at each instantaneous height during compression. Calculating the total energy stored in the origami structures as a function of the geometric parameters allows us to understand the folding behavior of the origami structures. The geometric parameter λ can significantly affect the energy change of the origami structures as shown in Fig. 2(*d*). Different energy change behaviors represent different folding behavior. If $\lambda = 0.6$, the origami structure only possesses one minimum energy state at initial state. Therefore, the total energy increases smoothly when the origami structure is compressed, indicating a monostable property. If the λ takes a larger value, such as 0.8 corresponding to the green line demarcated by positive triangle markers in Fig. 2(*d*), there are two local minimum states, meaning a bistable property. The larger the λ value, the more obvious the bistable property. Further, the stiffness of the structure can be obtained by calculating the second derivative of the energy. Although there are two geometric parameters (λ, N) that can significantly change the shape of the origami structure, by theoretical calculations, we find that only λ can have a considerable impact on its mechanical behavior, and the change of N will not affect the mechanical behavior of the structure, as shown in Fig. 2(*e*). This conclusion is confirmed again in subsequent experiments.

2.3 Experimental Validations. In order to verify the proposed theoretical model and accurately measure the mechanical properties of origami structures, several origami structures were manufactured and tested experimentally. The 2D sheets with creases patterns are first prepared, and laser cutter (EPILOG LASER mini 40) is used to cut card papers (180 g, LIANMU Co.) as previously prepared patterns. There are three kinds of lines in the illustration, as shown in Fig. 3(*a*). Black lines represent edges of 2D patterns and are cut off at 100% speed, 20% power, and 200 Hz frequency. The blue solid lines and red dashed lines represent mountain and valley creases, respectively. They are cut at 100% speed, 20% power, and 80 Hz frequency to form sprocket holes like postage stamps. After the sheet being cut into the desired pattern, as shown in Fig. 3(*b*), it is then folded along the creases with the red dashed lines forming valley creases and the blue solid lines forming mountain creases. Small trapezoid papers at the end of the side edge are folded to form a new plane, and the 3D origami structure can be maintained by gluing them together, as shown in Fig. 3(*c*).

In order to study the static properties of the origami structure, an electronic universal testing machine (KEXIN WDW-20) is used to perform uniaxial compression tests with displacement control. As described previously, the origami structure is a twist coupling structure, which means that compressing the origami structure will result in relative rotation of the upper and lower polygon surfaces. So, in order to obtain the authentic force–compression curve of origami structures in a free rotation environment, a special rotating platen with a double row angular contact ball bearing is designed and manufactured, as shown in Fig. 4(*a*). The rotating platen can support axial force but allow the free rotation of lower surfaces when fixing the upper surface. The loading speed was set to 10 mm/min

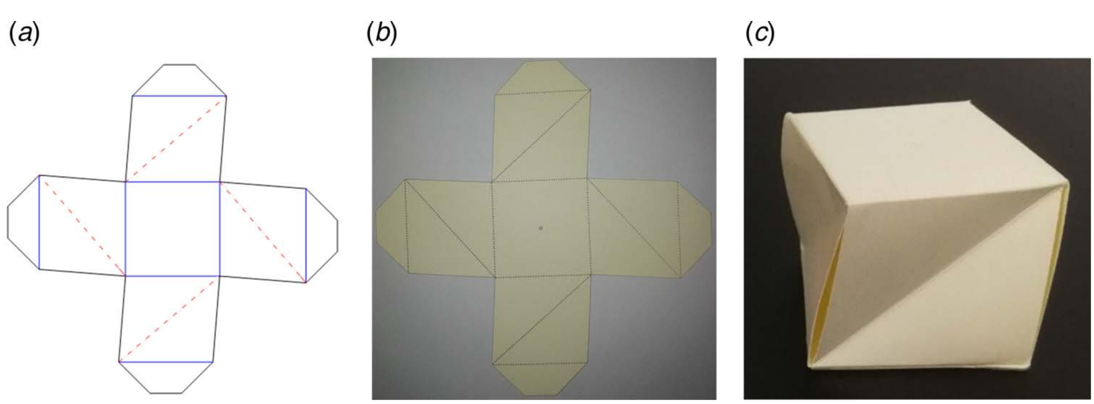

Fig. 3 (*a*) 2D design diagram with crease patterns, (*b*) the flat sheet cut with laser cutter, and (c) 3D origami structure (Color version online.)

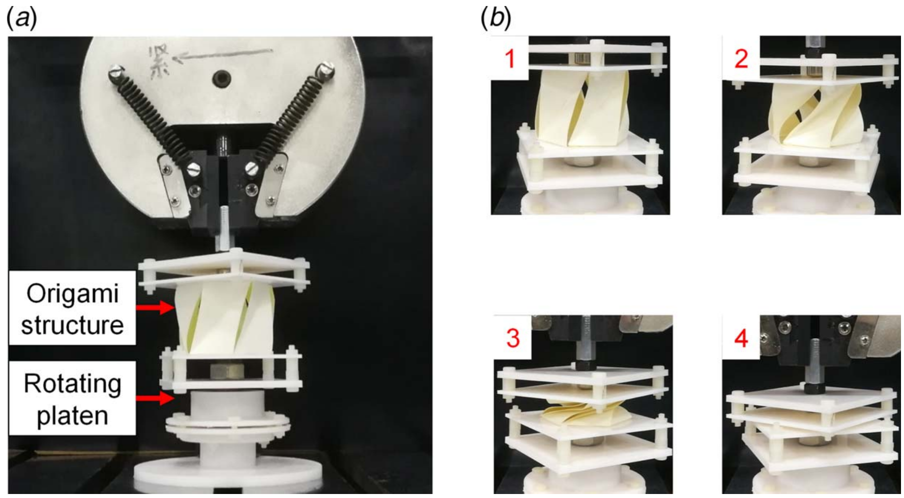

Fig. 4 **(*a*) Uniaxial compression experimental setup with the origami structure. (*b*) The origami structure at four instantaneous heights in a uniaxial compression experiment. The first and last images correspond to the fully expanded and folded state of the origami structure, respectively. From the figure, we can see that the side triangular plates of the origami structure are a generalized cone during compression.**

in all tests, and the conditions at the end of the test were set sufficiently large to ensure that the origami structure was completely folded at the end. During the experiment, the compression process of the origami structure was recorded with a camera to study the deformation of the origami structure.

N and λ are two important geometric parameters of the origami structure which can significantly change the geometric shapes of the structures. In order to explore the relationship between these two parameters and the static properties of the origami structure, we carry out uniaxial compression of the origami structure with different parameters. The experimental results are shown in Fig. 5 where the geometric parameter λ can be adjusted to significantly change the mechanical properties of the origami structure, as shown in Figs. 5(*a*) and 5(*b*). When λ equals to 0.6 or 0.7, the energy of the origami structure increases monotonically, implying monostable property. When λ equals to 0.8 or 0.9, the origami structure is bistable. However, the geometric parameter N does not significantly affect the mechanical properties of the origami structure, as shown in Figs. 5(*c*) and 5(*d*). These experimental results are in agreement with the theoretical results in Figs. 2(*d*) and 2(*e*).

3 Microstructure Design and Experimental Validation of One-Dimensional Origami-Based Metastructure

In this section, we study the flexural vibration isolation in the one-dimensional origami-based metastructure consisting of a Timoshenko beam and LR origami microstructures. The band structure of flexural wave propagation in the beam is calculated with the transfer matrix method. Also, we experimentally validated that the vibration isolation zone can be actively tuned through different stable states or geometrical parameter λ of the origami-based metastructure.

3.1 Theoretical Model of the One-Dimensional Metastructure. The vibration isolation ability of a Timoshenko beam with periodical LR structures has been investigated [15]. In this study, to form an adaptable bandgap, the unadjustable springs are replaced with the origami structures as shown in Fig. 6(*a*). First, for a simplified dynamic model, the tilting motion of the disc and the twist coupling of the origami structure are not considered. Therefore, the disc functions as a lumped mass with only translational motion in the vertical direction and the effect of the disc's shape can be ignored for the resonant frequency calculation, as shown in Fig. 6(*b*). Then, the governing equation for the Timoshenko beam can be written as follows:

$$\frac{EI}{\rho S}\frac{\partial^4 y(x,t)}{\partial x^4} - \frac{I}{S}\left(1+\frac{E}{\kappa G}\right)\frac{\partial^4 y(x,t)}{\partial x^2 \partial t^2} + \frac{\partial^2 y(x,t)}{\partial x^2} + \frac{\rho I}{\kappa G S}\frac{\partial^4 y(x,t)}{\partial t^4} = 0 \tag{10}$$

where ρ, E, and G are the density, Young's modulus, and shear modulus, respectively; S is the cross-sectional area; κ is the Timoshenko shear coefficient; and I is the area moment of inertia with respect to the axis perpendicular to the beam axis. Since only the steady-state response will be considered in this section, the bending deformation at x can be written as

$$y(x,t) = X(x)e^{i\omega t} \tag{11}$$

From Eqs. (10) and (11), the amplitude $X(x)$ of the bending displacement can be determined as

$$X(x) = Ak_1^{-3}e^{k_1 x} + Bk_2^{-3}e^{k_2 x} + Ck_3^{-3}e^{k_3 x} + Dk_4^{-3}e^{k_4 x} \tag{12}$$

where

$$k_j = (-1)^{[j/2]}\sqrt{[\alpha + (-1)^j\sqrt{\alpha^2+4\beta}]/2}, \quad j = 1, 2, 3, 4,$$

$$\alpha = -\frac{\rho\omega^2}{E} - \frac{\rho\omega^2}{\kappa G} \text{ and } \beta = \frac{\rho S\omega^2}{EI} - \frac{\rho^2\omega^4}{E\kappa G}$$

$[j/2]$ is the largest integer less than $j/2$.

For the nth unit cell, $X(x)$ can be written as

$$X_n(x') = A_n k_1^{-3}e^{k_1 x'} + B_n k_2^{-3}e^{k_2 x'} + C_n k_3^{-3}e^{k_3 x'} + D_n k_4^{-3}e^{k_4 x'} \tag{13}$$

where $x' = x - na$, $na \le x \le (n+1)a$. The equilibrium condition for the nth resonator along the vertical direction is

$$f_n(t) - m\ddot{Z}_n(t) = 0 \tag{14}$$

where $f_n(t)$ is the interactive force between the local resonator and the beam, and $Z_n(t) = V_n e^{i\omega t}$ is the displacement of the nth local resonator at the position $x = na$. Then, the interactive force can be calculated as

$$f_n(t) = k[y(x_n,t) - Z_n(t)] = k[X_n(0) - V_n]e^{i\omega t} = F_n e^{i\omega t} \tag{15}$$

where k is the effective spring stiffness of the origami structures, which is a function of the origami structure's geometric parameter

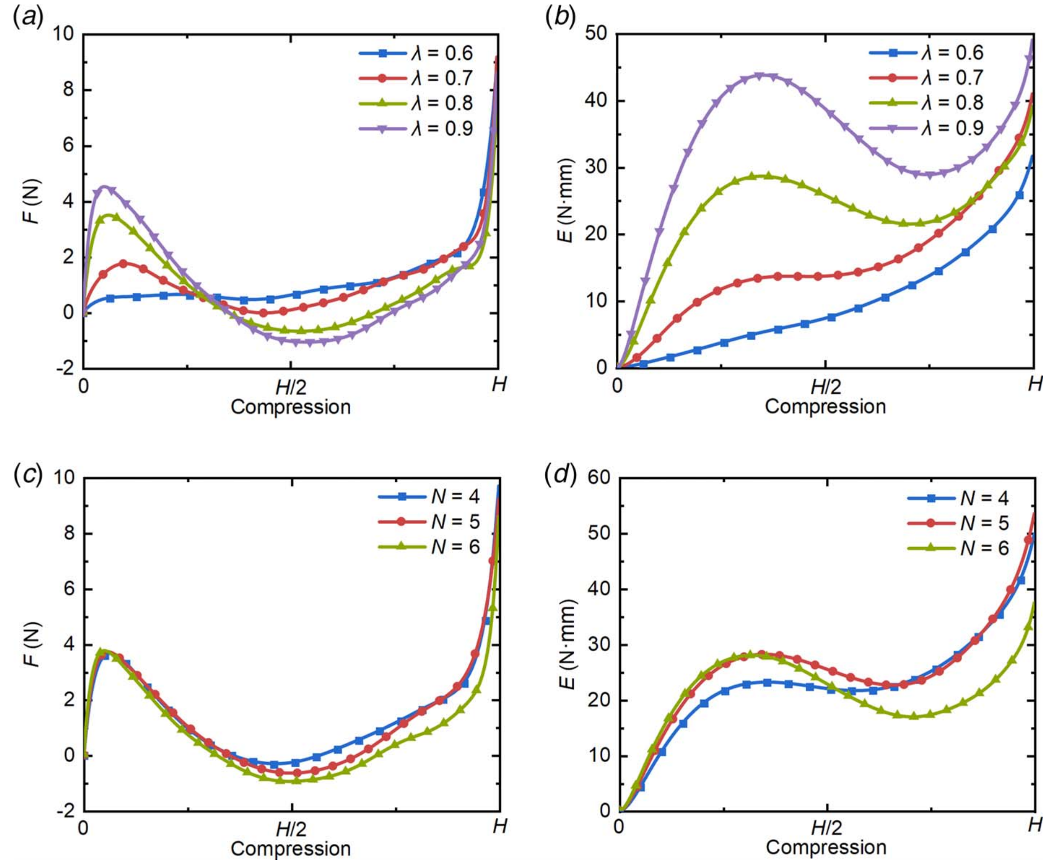

Fig. 5 Results of the uniaxial compression test of the origami structure: (*a*) force–compression response of origami structures with $N=4$ and $R=42.4$ mm for various λ values, (*b*) energy–compression response of origami structures with $N=4$ and $R=42.4$ mm for various λ values, (*c*) force–compression response of origami structures with $\lambda=0.9$ and $R=30$ mm for various N values, and (*d*) energy–compression response of origami structures with $\lambda=0.9$ and $R=30$ mm for various N values

λ at its current stable state. To be specific, the energy–compression curve is first calculated with the theoretical method introduced in Sec. 2.2. Then, the effective spring constant is obtained by calculating the second derivative of the energy with respect to the compression. Substituting Eq. (15) into Eq. (14) leads to

$$V_n = \frac{k}{k - m\omega^2} X_n(0) \tag{16}$$

Applying the continuity conditions of displacement, displacement gradient, bending moment, and shear force at the interface between nth and $(n-1)$th cell, we have

$$X_n(0) = X_{n-1}(a) \tag{17a}$$

$$X'_n(0) = X'_{n-1}(a) \tag{17b}$$

$$EIX''_n(0) = EIX''_{n-1}(a) \tag{17c}$$

$$EIX'''_n(0) - F_n = EIX'''_{n-1}(a) \tag{17d}$$

Substituting Eqs. (13), (15), and (16) into Eq. (17), the following equation can be obtained:

$$\mathrm{K}\Psi_n = \mathrm{H}\Psi_{n-1} \tag{18}$$

where

$$\mathbf{K} = \begin{bmatrix} k_1^{-3} & k_2^{-3} & k_3^{-3} & k_4^{-3} \\ k_1^{-2} & k_2^{-2} & k_3^{-2} & k_4^{-2} \\ k_1^{-1} & k_2^{-1} & k_3^{-1} & k_4^{-1} \\ 1 + Fk_1^{-3} & 1 + Fk_2^{-3} & 1 + Fk_3^{-3} & 1 + Fk_4^{-3} \end{bmatrix} \tag{19}$$

$$\mathbf{H} = \begin{bmatrix} k_1^{-3}e^{k_1 a} & k_2^{-3}e^{k_2 a} & k_3^{-3}e^{k_3 a} & k_4^{-3}e^{k_4 a} \\ k_1^{-2}e^{k_1 a} & k_2^{-2}e^{k_2 a} & k_3^{-2}e^{k_3 a} & k_4^{-2}e^{k_4 a} \\ k_1^{-1}e^{k_1 a} & k_2^{-1}e^{k_2 a} & k_3^{-1}e^{k_3 a} & k_4^{-1}e^{k_4 a} \\ e^{k_1 a} & e^{k_2 a} & e^{k_3 a} & e^{k_4 a} \end{bmatrix} \tag{20}$$

$$\Psi_n = \begin{bmatrix} A_n \\ B_n \\ C_n \\ D_n \end{bmatrix} \tag{21}$$

$$F = \frac{-1}{EI} \frac{mk\omega^2}{k - m\omega^2} \tag{22}$$

Based on Eq. (18), the wave transfer relation between the nth cell and $(n-1)$th cell can be given as

$$\Psi_n = \mathbf{T}\Psi_{n-1} \tag{23}$$

where $\mathbf{T} = \mathbf{K}^{-1}\mathbf{H}$ is the transfer matrix between the two adjacent cells.

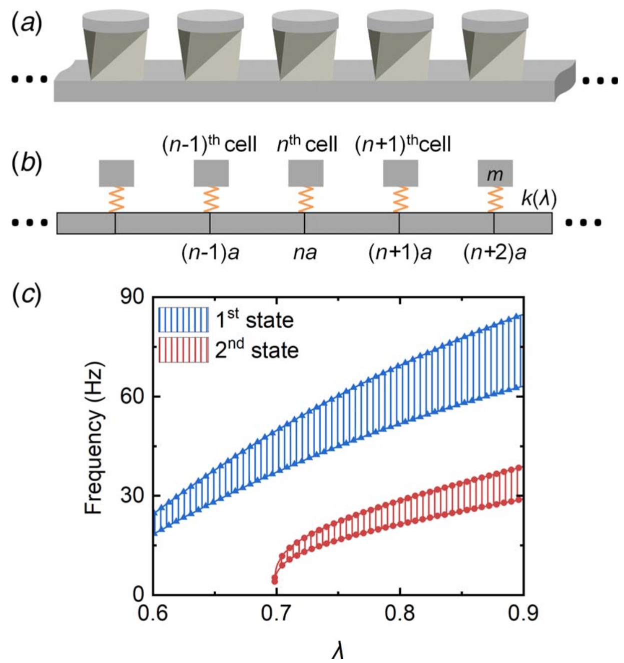

Fig. 6 (*a*) The 3D model of a beam with origami-based LR structures, (*b*) the simplified model, and (*c*) bandgap control by the stable states and geometric parameter λ of origami. The lines demarcated by blue triangle markers, and red circle markers represent the edges of the bandgap corresponding to the first and second stable state of the origami structures, respectively. (Color version online.)

To calculate the band structure of the metastructure, Bloch theorem can be applied to the boundaries of the unit cell as

$$\Psi_n = e^{iqa}\Psi_{n-1} \tag{24}$$

where q is the wavenumber in the x-direction. From Eqs. (23) and (24), we can obtain the eigen-value problem

$$|\mathbf{T} - e^{iqa}\mathbf{I}| = 0 \tag{25}$$

From which the band structure can be determined. Naturally, the bandgap of the origami-based beam can be adjusted by manufacturing origami structures with different λ as shown in Fig. 6(*c*). Specifically, when λ is large than 0.7, bistable structures can be obtained which will provide a unique way to switch stable state and adjust the bandgap in situ.

Based on the transfer matrix $\mathbf{T}$, in Eq. (23), the transmission behavior of a metastructure beam containing ten origami unit cells is studied. Bistable origami unit cells ($N = 4$, $\lambda = 0.9$) is used in this case to demonstrate the adjustability of the metastructure beam. The effective stiffness of the two stable states of the origami structures can be obtained from the previous static experiments. In Fig. 7, a displacement excitation is applied at the left end of the finite beam and the frequency response function (FRF), which is defined as the ratio between the right end displacement response and the excitation as a function of frequency, can be obtained by setting the boundary conditions as

$$X_0(0) = u_0 \tag{26a}$$

$$X_n'(0) = 0 \tag{26b}$$

$$EIX_N''(a) = 0 \tag{26c}$$

$$EIX_N'''(a) = 0 \tag{26d}$$

Here, the harmonic excitation displacement, u_0, is applied to the left end of the finite beam along transverse direction and the right end of the beam is free.

The FRFs of the metastructure beams containing the same stable-state unit cells are first investigated. First, it is shown in Fig. 7(*c*) that the vibration isolation regions appear in the shaded areas. Second, by switching from the first stable state to the second stable state, the second resonance peak of the solid blue curve disappears, which falls into the vibration isolation region at the second stable state (red shaded area). Third, new resonance peaks appear on both sides of the vibration isolation zones for the metastructure beam, which is due to the positively enlarged vibrations (can also be explained by zero effective mass density before and after the negative effective mass density region) happened before and after the origami cells' LR frequency ranges. These phenomena can also be observed in the experiment results (in Fig. 10(*b*)). Further, the FRFs of two kinds of hybrid combinations are also studied, as shown in Figs. 7(*d*)–7(*f*). In one combination, two sections of different unit cells can be found in the metastructure beam, where the left and right sections consist of five first stable-state and five second stable-state origami structures, respectively, as shown in Fig. 7(*d*). In the other combination, the first stable state and second stable state arranged alternately, as shown in Fig. 7(*e*). By comparing the FRF results of the two combinations, it can be found that both combinations have two vibration isolation zones which are caused by the resonance of the first stable state and second stable state, respectively. Also, the way that the mass being placed on each resonator significantly affects the metastructure beam response, which is investigated numerically in Appendix B.

3.2 Experimental Validation. In order to make the origami-based metastructure beam have adjustable vibration isolation ability, bistability as well as adjustable stiffness are designed in each unit cell. By gluing the origami microstructure ($N = 4$, $R = 28.3$ mm) with a mass disk, the resonant unit cell of the metastructure is fabricated. The lattice constant is 78 mm, the thickness of the mass disk is 5 mm, radius is 28.3 mm, and the material of the disc is aluminum, with the same material parameters as the beam (Table 1). Figure 8(*a*) shows two different stable states of a unit cell. The origami unit cells are periodically arranged on beams to make one-dimensional metastructures. The experimental setup for the vibration test is shown in Fig. 8(*b*). The beam is fixed on a shaker (LDS V406) which is powered by a power amplifier (LDS LPA600). White noise excitation signal with bandwidth from 0 to 250 Hz is generated by the shaker. The response of the beam is captured by an accelerometer which is attached to the other end of the beam. Both input signal and output signal are processed by the dynamic analyzer (Dactron PHOTON+™) and transmitted to the PC. The amplitude transmission coefficient is defined as the ratio of the output signal from the accelerometer with respect to the input signal from the shaker.

An FE-based metastructure beam with origami-based local resonant unit cells is first built and investigated from comparison purposes, as shown in Fig. 9(*a*). A force excitation is applied at the left end of the beam, while the acceleration response at the right end is calculated. The FRF is defined as the ratio of the acceleration response with response to the force excitation as a function of frequency. In order to validate the FE result, the vibration isolation zones calculated by FE and theoretical models are compared in Fig. 9(*b*). It can be found that the lower edge of the vibration isolation zone fits well. But, the upper edge of the vibration isolation zone has some deviations, which is due to the fact that the masses are point-connected to the beam by springs in the theoretical model, while the mass discs are face-contacted to the beam by origami unit cells in the FE model. In addition, there will be significant friction and damping in the experiments. In order to compensate that the effect of damping is studied and an FE model with damping ratio $\zeta = 0.1$ is established. After introducing the

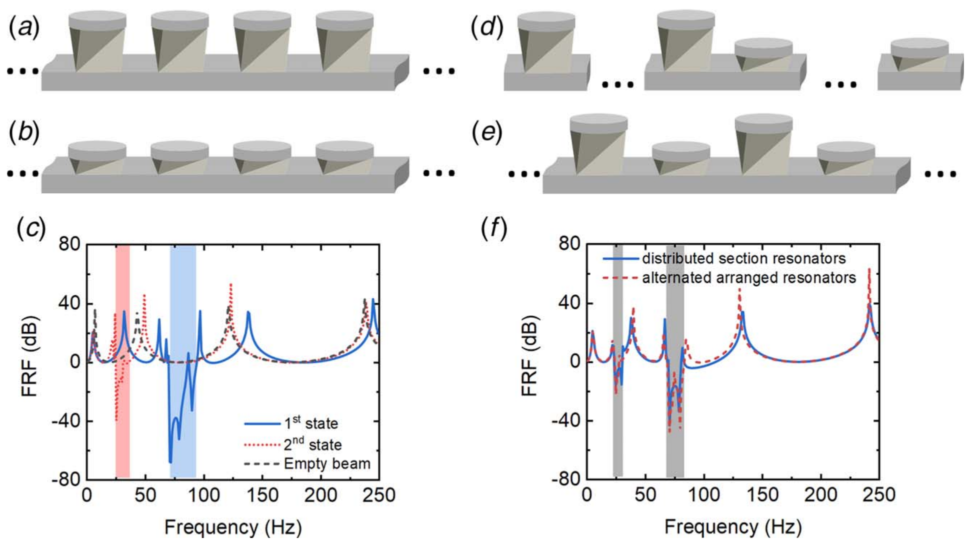

Fig. 7 The 3D model of a beam with (*a*) first stable state and (*b*) second stable state of the origami structures. (c) FRFs of the finite metastructure beams from the transfer matrix method. The black dashed line, the blue solid line, and the red dotted line represent the FRF of the empty beam, metastructure beam with first state origami structures and second state origami structures, respectively. (*d*) The 3D model of a beam with two sections. Left section consists of five first stable-state origami structures, and right section consists of five second stable-state origami structures. (e) The 3D model of a beam with ten origami structures which first stable state and second stable state arranged alternately. (*f*) FRFs of the finite metastructure beams from the transfer matrix method. The blue solid line and the red dotted line represent the FRF of the metastructure beam shown in (*d* and e), respectively. The vibration isolation zones are highlighted by the shaded areas. (Color version online.)

Table 1 Geometrical and material parameters of the beam

Geometrical parameters	Material parameters
Thickness $t = 5$ mm	Young's modulus 68.9 GPa
Width $b = 40$ mm	Mass density 2670 kg/m^3
Length $L = 800$ mm	Poisson's ratio 0.33

damping, the FE result is in good agreement with the experimental result, as shown in Fig. 9(*c*). The numerical simulation is performed by using the commercial finite-element software ANSYS 18.2.

Figure 10 demonstrates the experimental results of the vibration tests on the manufactured metastructure beams. Figure 10(*a*) illustrates the measured stiffness–compression curves for $\lambda = 0.9$ and $\lambda = 0.7$ unit cells. The three states represented by the blue, green, and purple dots are marked on the curves, which are corresponding to the first stable state of the $\lambda = 0.9$ unit cell, the second stable state of the $\lambda = 0.9$ unit cell, and the monostable state of the $\lambda = 0.7$ unit cell, respectively. The highlighted regions are the identified metastructure's vibration isolation zones by comparing with the transmission result of the empty beam with no local resonators, as shown in Figs. 10(*b*) and 10(*c*). To be specific, the position of the vibration isolation zone is determined by looking for the lowest valley below the empty beam and the vertices of valley or the intersection points with empty beam are used as criterions for the edges of the vibration isolation zone. Figure 10(*b*) compares the measured transmission results obtained from the

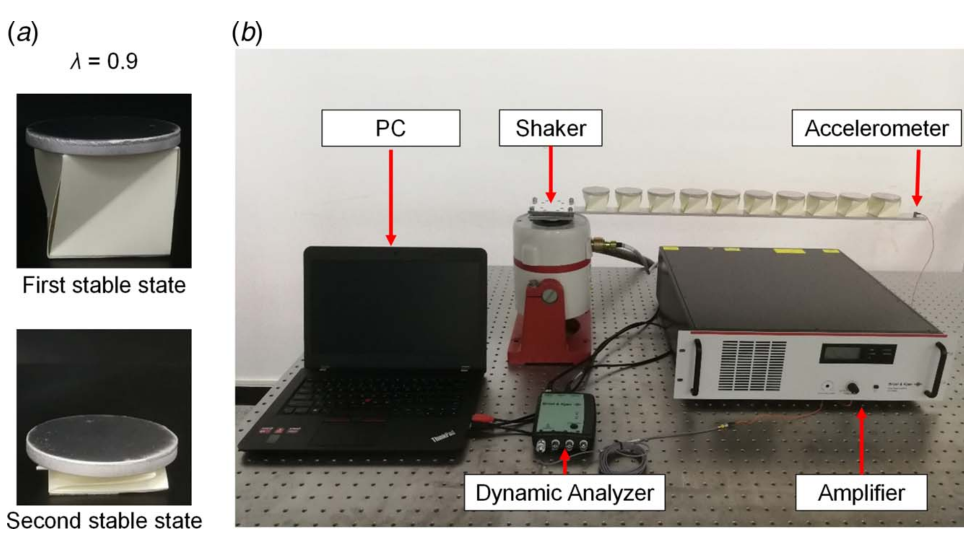

Fig. 8 (*a*) First and second stable states of the origami unit cell and (*b*) 1D origami-based metastructure and the vibration test setup

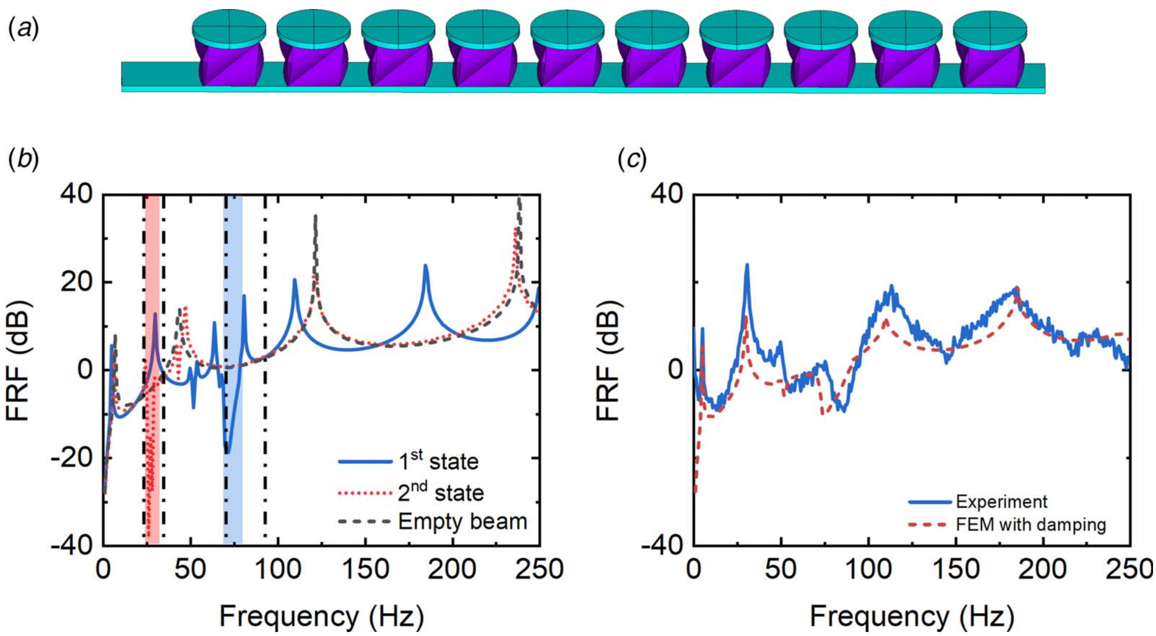

Fig. 9 (a) A practical structural model of the metastructure beam with origami-based local resonant unit cells. (b) FRFs of the finite metastructure beams from FE method without damping. The black dashed line, the blue solid line, and the red dotted line represent the FRF of the empty beam, metastructure beam with first state origami structures and second state origami structures, respectively. The vibration isolation zones are highlight by the shaded areas. The lower and upper edges of the theoretical vibration isolation zones are marked with black dash-dotted lines, and (c) FRFs of the finite metastructure beams considering damping. The blue solid line and red dashed line represent the experimental result and FE result, respectively. (Color version online.)

metastructure beam with the $\lambda = 0.9$ unit cell at the first stable state and that at the second stable state. It can be found that the vibration isolation zone moves to the lower frequency range when the unit cell switches from the large stiffness state (first stable state) to the low stiffness state (second stable state). The same trend can be found when comparing the results of metastructure with decreasing λ (lower stiffness) units, as shown in Fig. 10(*c*). With the effective stiffness of origami structures in Fig. 10(*a*), the theoretical vibration isolation zones (marked with red dashed lines) can be obtained. For the lower edges of the vibration isolation zones, good agreements between theoretical and experimental results can be found. However, due to the material dissipation and friction-induced structure damping which is not considered in the theoretical model, the width of vibration isolation zones measured by the experiment is larger than those obtained from the theoretical model [34]. Particularly, for the second stable state of the $\lambda = 0.9$ unit cell, the folded structure brings intense friction between the papers which will aggravate the damping effect of the structure, which result in significantly wider zone than that obtained theoretically.

4 Origami-Based Metastructure Plate

In this section, the origami cells are arranged periodically in a two-dimensional fashion to form a plate-like metastructure, as shown in Fig. 11. The vibration shapes of the metastructure plate under

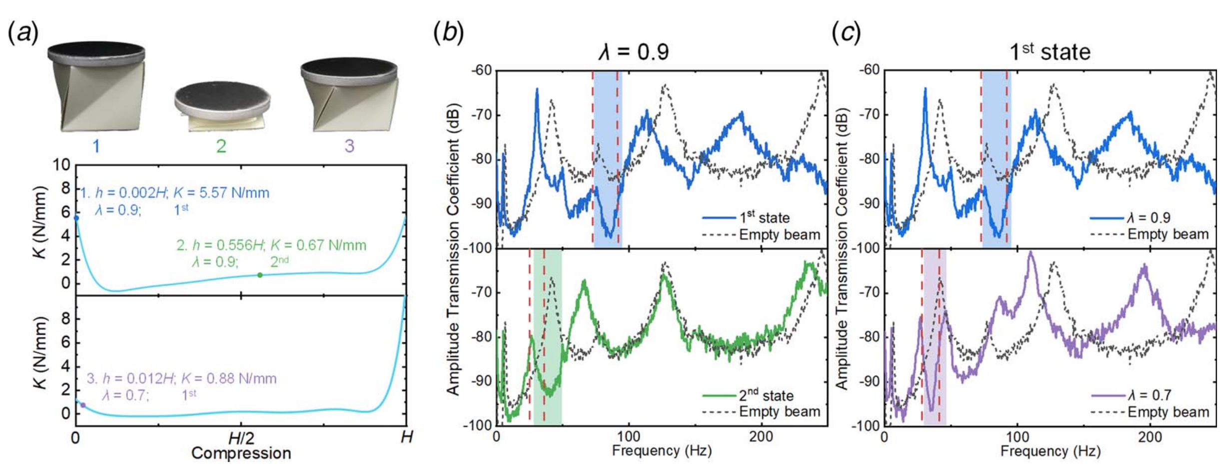

Fig. 10 (a) Stiffness–compression curve and (b and c) experimentally measured amplitude–frequency curves of origami-based metastructure. The test result drawn with blue, green, and purple correspond to states 1, 2, and 3 in (a), respectively. The black dashed line corresponds to the test result of empty beam. The vibration isolation zones measured experimentally are highlighted with shaded areas. The lower and upper edges of the theoretical vibration isolation zones are marked with red dashed lines. (Color version online.)

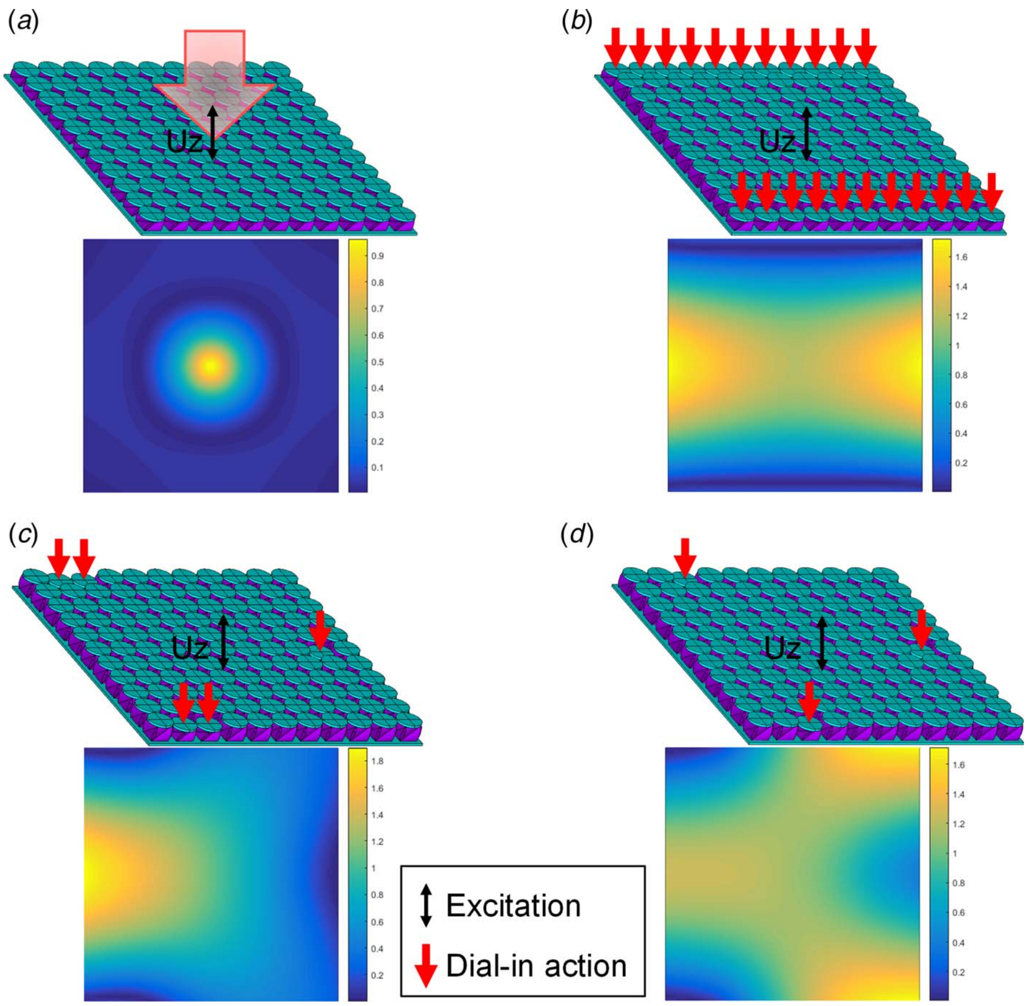

Fig. 11 Different vibration shapes of 2D origami-based plate-like metastructure

forced vibration are investigated. The sides of the plate are free, and an out-of-plane displacement excitation is applied at the center of the plate with an excitation frequency of 28 Hz which falls right in the vibration isolation zone for second stable state. When all the unit cells are in the second stable state, the wave stops propagating omnidirectionally, as shown in Fig. 11(*a*). Thanks to the bistability, we can independently adjust the stable state of each unit cell and, therefore, form a custom-designed plate vibration shape. It is also very easy to switch the unit cells' stable states by just dialing in or out the origami structures. Therefore, one can change the pattern of the 2D metastructure as we want. Here, we demonstrate that the number of axes of symmetry of vibration shapes can be changed accordingly by adjusting certain origami unit cells. Figure 11(*b*) shows the vibration shape with two axes of symmetry, while Figs. 11(*c*) and 11(*d*) show the two different vibration shapes with only one axis of symmetry. It can be seen that the vibration mode of the metamaterial plate can be controlled by the attached origami units above.

5 Conclusions

In the study, a prismatic bistable origami unit was introduced in the design of metastructures for vibration control purposes. With the adjustable origami unit, a 1D beam-like metastructure was fabricated with its vibration isolation zone being actively tuned through different compression loadings. A 2D plate-like metastructure was also designed and numerically studied for the control of different vibration modes. The proposed origami-based metastructures can be potentially useful in various engineering applications where structures with and vibration-proof abilities are appreciated.

Acknowledgment

R. Z. thanks for the financial support from the National Natural Science Foundation of China (Grants No. U1837602, 11872112, and 11991033), 111 Project (B16003), and the startup funding of Beijing Institute of Technology, China (Grant No. 2018CX01031).

Conflict of Interest

There are no conflicts of interest.

Data Availability Statement

The datasets generated and supporting the findings of this article are obtainable from the corresponding author upon reasonable request. The authors attest that all data for this study are included in the paper.

Appendix A: Measurement of the Effective Stiffness of Creases

The effective stiffness of the creases is very important for the carrying capacity of the origami structure and also affects the mechanical properties of the proposed metastructure. However, the bending motion of the creases induces plastic deformation which makes the accurate determination of the crease's stiffness very difficult in an analytical way. Therefore, we design an experimental device, as shown in Fig. 12, for the crease's stiffness measurement. In the

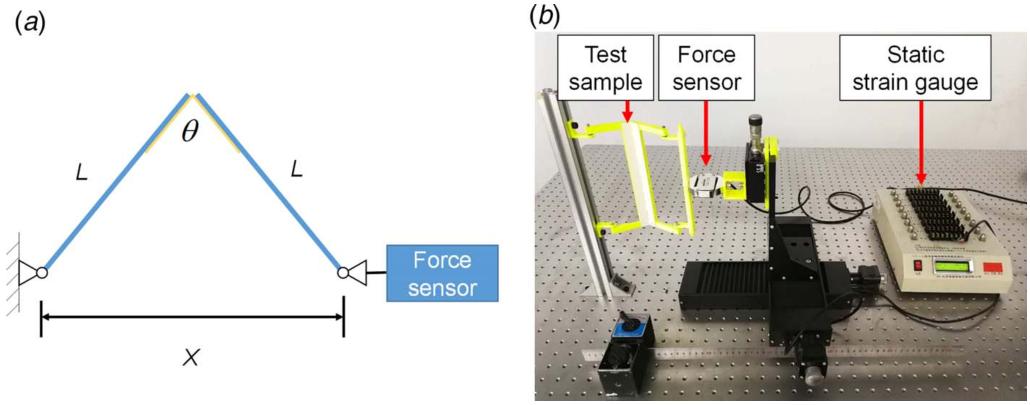

Fig. 12 (*a*) Experimental schematic: the yellow fold line represents the paper with creases, the corner is the position of the crease, and the blue solid line represents the rigid support structure and (*b*) experimental setup (Color version online.)

experiment, moment applied to the crease can be calculated by $M = FL\cos(\theta)$, where F is measured by force sensor (KT-5KG). The angle of the crease can be calculated by $\theta = \arcsin(X/(2L))$, where X can be directly measured. Therefore, the effective stiffness of the crease can be obtained as $k_c = M/\theta$.

Appendix B: The Effect of Additional Mass on Metastructure Beam Response

In order to study the effect of the mass placed on resonators on the behavior of metamaterial beam, we calculated the FRFs of the finite metastructure beams which have different attached mass discs as shown in Fig. 13. If the mass of the discs is reduced, the vibration isolation zone of the metamaterial beam moves to high frequency region. On the other hand, the metamaterial beam has a lower frequency vibration isolation region when the mass of the discs is increased.

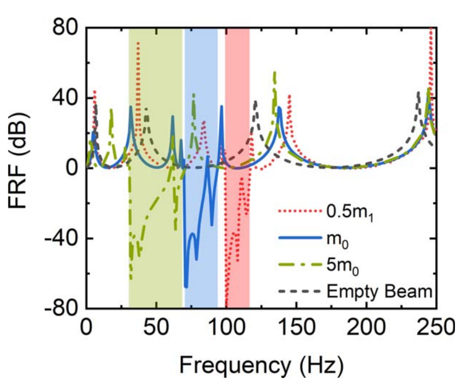

Fig. 13 FRFs of the finite metastructure beams from the transfer matrix method. The black dashed line, the blue solid line, the red dotted line, and green dash-dotted line represent the FRF of the empty beam, metastructure beams with m_0, $0.5m_0$, and $5m_0$ attached massed discs, respectively. The vibration isolation zones are highlight by the color blocks. (Color version online.)

References

[1] Sihvola, A., 2007, "Metamaterials in Electromagnetics," Metamaterials, **1**(1), pp. 2–11.
[2] Liu, Z., Zhang, X., Mao, Y., Zhu, Y. Y., Yang, Z., Chan, C. T., and Sheng, P., 2000, "Locally Resonant Sonic Materials," Science, **289**(5485), pp. 1734–1736.
[3] Yao, S., Zhou, X., and Hu, G., 2008, "Experimental Study on Negative Effective Mass in a 1D Mass–Spring System," New J. Phys., **10**(4), p. 043020.
[4] Liu, Z., Chan, C. T., and Sheng, P., 2005, "Analytic Model of Phononic Crystals With Local Resonances," Phys. Rev. B, **71**(1), p. 014103.
[5] Zhu, R., Liu, X. N., Hu, G. K., Sun, C. T., and Huang, G. L., 2014, "Negative Refraction of Elastic Waves at the Deep-Subwavelength Scale in a Single-Phase Metamaterial," Nat. Commun., **5**(1), p. 5510.
[6] Liu, X. N., Hu, G. K., Huang, G. L., and Sun, C. T., 2011, "An Elastic Metamaterial With Simultaneously Negative Mass Density and Bulk Modulus," Appl. Phys. Lett., **98**(25), p. 251907.
[7] Scheibner, C., Souslov, A., Banerjee, D., Surowka, P., Irvine, W. T., and Vitelli, V., 2020, "Odd Elasticity," Nat. Phys., **16**(4), pp. 475–480.
[8] Frenzel, T., Kadic, M., and Wegener, M., 2017, "Three-Dimensional Mechanical Metamaterials With a Twist," Science, **358**(6366), pp. 1072–1074.
[9] Coulais, C., Sounas, D., and Alù, A., 2017, "Static Non-Reciprocity in Mechanical Metamaterials," Nature, **542**(7642), pp. 461–464.
[10] Zhu, R., Liu, X. N., Hu, G. K., Sun, C. T., and Huang, G. L., 2014, "A Chiral Elastic Metamaterial Beam for Broadband Vibration Suppression," J. Sound Vib., **333**(10), pp. 2759–2773.
[11] Chen, J. S., Sharma, B., and Sun, C. T., 2011, "Dynamic Behaviour of Sandwich Structure Containing Spring-Mass Resonators," Compos. Struct., **93**(8), pp. 2120–2125.
[12] Yu, T., and Lesieutre, G. A., 2017, "Damping of Sandwich Panels via Three-Dimensional Manufactured Multimode Metamaterial Core," AIAA J., **55**(4), pp. 1440–1449.
[13] Cai, C., Zhou, J., Wu, L., Wang, K., Xu, D., and Ouyang, H., 2020, "Design and Numerical Validation of Quasi-Zero-Stiffness Metamaterials for Very Low-Frequency Band Gaps," Compos. Struct., **236**, p. 111862.
[14] Huang, H. H., Sun, C. T., and Huang, G. L., 2009, "On the Negative Effective Mass Density in Acoustic Metamaterials," Int. J. Eng. Sci., **47**(4), pp. 610–617.
[15] Yu, D., Liu, Y., Wang, G., Zhao, H., and Qiu, J., 2006, "Flexural Vibration Band Gaps in Timoshenko Beams With Locally Resonant Structures," J. Appl. Phys., **100**(12), p. 124901.
[16] Zhu, R., Huang, G. L., Huang, H. H., and Sun, C. T., 2011, "Experimental and Numerical Study of Guided Wave Propagation in a Thin Metamaterial Plate," Phys. Lett. A, **375**(30–31), pp. 2863–2867.
[17] Miranda, E. J. P., Jr., Nobrega, E. D., Ferreira, A. H. R., and Dos Santos, J. M. C., 2019, "Flexural Wave Band Gaps in a Multi-Resonator Elastic Metamaterial Plate Using Kirchhoff-Love Theory," Mech. Syst. Sig. Process., **116**, pp. 480–504.
[18] Pai, P. F., 2010, "Metamaterial-Based Broadband Elastic Wave Absorber," J. Intell. Mater. Syst. Struct., **21**(5), pp. 517–528.
[19] Chen, H., Li, X. P., Chen, Y. Y., and Huang, G. L., 2017, "Wave Propagation and Absorption of Sandwich Beams Containing Interior Dissipative Multi-Resonators," Ultrasonics, **76**, pp. 99–108.
[20] Bergamini, A., Delpero, T., Simoni, L. D., Lillo, L. D., Ruzzene, M., and Ermanni, P., 2014, "Phononic Crystal With Adaptive Connectivity," Adv. Mater., **26**(9), pp. 1343–1347.
[21] Chen, Y. Y., Huang, G. L., and Sun, C. T., 2014, "Band Gap Control in an Active Elastic Metamaterial With Negative Capacitance Piezoelectric Shunting," ASME J. Vib. Acoust., **136**(6), p. 061008.
[22] Zhu, R., Chen, Y. Y., Barnhart, M. V., Hu, G. K., Sun, C. T., and Huang, G. L., 2016, "Experimental Study of an Adaptive Elastic Metamaterial Controlled by Electric Circuits," Appl. Phys. Lett., **108**(1), p. 011905.
[23] Li, X., Chen, Y., Hu, G., and Huang, G., 2018, "A Self-Adaptive Metamaterial Beam With Digitally Controlled Resonators for Subwavelength Broadband Flexural Wave Attenuation," Smart Mater. Struct., **27**(4), p. 045015.
[24] Overvelde, J. T. B., De Jong, T. A., Shevchenko, Y., Becerra, S. A., Whitesides, G. M., Weaver, J. C., Hoberman, C., and Bertoldi, K., 2016, "A Three-Dimensional Actuated Origami-Inspired Transformable Metamaterial With Multiple Degrees of Freedom," Nat. Commun., **7**(1), p. 10929.

[25] Overvelde, J. T., Weaver, J. C., Hoberman, C., and Bertoldi, K., 2017, "Rational Design of Reconfigurable Prismatic Architected Materials," Nature, **541**(7637), pp. 347–352.
[26] Chen, Y., Peng, R., and You, Z., 2015, "Origami of Thick Panels," Science, **349**(6246), pp. 396–400.
[27] Novelino, L. S., Ze, Q., Wu, S., Paulino, G. H., and Zhao, R., 2020, "Untethered Control of Functional Origami Microrobots With Distributed Actuation," Proc. Natl. Acad. Sci. U. S. A., **117**(39), pp. 24096–24101.
[28] Zhai, Z., Wang, Y., and Jiang, H., 2018, "Origami-Inspired, On-Demand Deployable and Collapsible Mechanical Metamaterials With Tunable Stiffness," Proc. Natl. Acad. Sci. U. S. A., **115**(9), pp. 2032–2037.
[29] Fang, H., Zhang, Y., and Wang, K. W., 2017, "Origami-Based Earthworm-Like Locomotion Robots," Bioinspir. Biomim., **12**(6), p. 065003.
[30] Yasuda, H., Tachi, T., Lee, M., and Yang, J., 2017, "Origami-Based Tunable Truss Structures for Non-Volatile Mechanical Memory Operation," Nat. Commun., **8**(1), pp. 862.
[31] Babaee, S., Pajovic, S., Rafsanjani, A., Shi, Y., Bertoldi, K., and Traverso, G., 2020, "Bioinspired Kirigami Metasurfaces as Assistive Shoe Grips," Nat. Biomed. Eng., **4**(8), pp. 778–786.
[32] Yasuda, H., and Yang, J., 2015, "Reentrant Origami-Based Metamaterials With Negative Poisson's Ratio and Bistability," Phys. Rev. Lett., **114**(18), p. 185502.
[33] Yang, N., Zhang, M., and Zhu, R., 2020, "3D Kirigami Metamaterials With Coded Thermal Expansion Properties," Extreme Mech. Lett., **40**, p. 100912.
[34] Manimala, J. M., and Sun, C. T., 2014, "Microstructural Design Studies for Locally Dissipative Acoustic Metamaterials," J. Appl. Phys., **115**(2), p. 023518.